RESEARCH ARTICLE | MARCH 05 2018

Reaction pathways of producing and losing particles in atmospheric pressure methane nanosecond pulsed needle-plane discharge plasma

Yuefeng Zhao; Chao Wang; Li Li; Lijuan Wang; Jie Pan ✉

Phys. Plasmas 25, 033504 (2018)
https://doi.org/10.1063/1.5018667

Reaction pathways of producing and losing particles in atmospheric pressure methane nanosecond pulsed needle-plane discharge plasma

Yuefeng Zhao,[1] Chao Wang,[1] Li Li,[2] Lijuan Wang,[1] and Jie Pan[1,a)]
[1]School of Physics and Electronics, Shandong Normal University, Jinan 250014, China
[2]State Grid Jinan Power Supply Company, Jinan 250012, China

(Received 8 December 2017; accepted 20 February 2018; published online 5 March 2018)

In this work, a two-dimensional fluid model is built up to numerically investigate the reaction pathways of producing and losing particles in atmospheric pressure methane nanosecond pulsed needle-plane discharge plasma. The calculation results indicate that the electron collisions with CH_4 are the key pathways to produce the neutral particles CH_2 and CH as well as the charged particles e and CH_3^+. CH_3, H_2, H, C_2H_2, and C_2H_4 primarily result from the reactions between the neutral particles and CH_4. The charge transfer reactions are the significant pathways to produce CH_4^+, $C_2H_2^+$, and $C_2H_4^+$. As to the neutral species CH and H and the charged species CH_3^+, the reactions between themselves and CH_4 contribute to substantial losses of these particles. The ways responsible for losing CH_3, H_2, C_2H_2, and C_2H_4 are $CH_3 + H \rightarrow CH_4$, $H_2 + CH \rightarrow CH_2 + H$, $CH_4^+ + C_2H_2 \rightarrow C_2H_2^+ + CH_4$, and $CH_4^+ + C_2H_4 \rightarrow C_2H_4^+ + CH_4$, respectively. Both electrons and $C_2H_4^+$ are consumed by the dissociative electron-ion recombination reactions. The essential reaction pathways of losing CH_4^+ and $C_2H_2^+$ are the charge transfer reactions. https://doi.org/10.1063/1.5018667

I. INTRODUCTION

As the main ingredient of natural gas, marsh gas, and mine gas, methane (CH_4) is the raw material to generate hydrogen, carbon black, carbon monoxide, formaldehyde, and acetylene and the essential fuel for civil and industrial heating. Furthermore, CH_4 has widely received attention and applications in fields such as crop fertilization, gas power generation, synthesis gas production, and nanomaterial synthesis.[1,2] The heavy oil hydrogenation technique is a promising way to make full use of hydrocarbon because it can translate heavy oil into light oil by dealing with inferior crude oil. As a result of employing catalyst and near hydrogen environment under the conditions of high gas pressure and high temperature, the traditional heavy oil hydrogenation technique has a few shortcomings, i.e., high energy consumption, low light oil yield, and the catalyst being easy to coke. Previous research has indicated that the nanosecond pulsed discharge can produce high chemical activity and non-equilibrium discharge plasma under a wide range of the gas pressures.[3–7] By combining the methane nanosecond pulsed discharge with the traditional heavy oil hydrogenation, the methane plasma conversion heavy oil hydrogenation technique may realize the high efficiency heavy oil hydrogenation and increase the production of the high value-added low carbon olefins, which have extensive application prospects and important research significance.

Methane conversion in discharge plasma is an emerging topic in the realm of low temperature plasma. Bogaerts *et al.* have investigated influences of N_2 concentration in the CH_4/N_2 dielectric barrier discharge (DBD) on the CH_4 conversion into H_2.[8] Tu and Whitehead have developed an alternating-current (AC) gliding arc reactor to offer the novel route for the co-generation of syngas and value-added carbon nanomaterials by plasma dry reforming of methane.[9] Bie *et al.* have studied the dominated pathways for methane conversion into oxygenates and syngas in atmospheric pressure DBD using a one-dimensional numerical model.[10] Park *et al.* have explored conversions of CH_4 and CO_2, energy efficiency, and syngas energy cost in CH_4/CO_2 AC-pulsed tornado gliding arc plasma.[11] Indarto has achieved high yield production of methanol by a single-stage plasma reactor from non-catalytic conversions of CH_4 and NO_2.[12] Recently, Fridman *et al.* have applied nanosecond pulsed DBD at atmospheric pressure and atmospheric pressure glow discharge (APGD) to directly incorporate methane into liquid fuel, and preliminary results have indicated that both discharges cause CH_4 reaction with liquid fuel and fixation of CH_4 in liquid fuel.[13] This research has illustrated that the low temperature discharge plasma can provide new approaches to high efficiency CH_4 conversion and heavy oil hydrogenation. And, however, in the above publications, CH_4 direct conversions based on discharge plasmas mainly employ DBD, APGD, or gliding arc discharge. In CH_4 reforming using DBD, both discharge and afterglow play an important role, and thus the CH_4 dissociation by the single streamer discharge has attracted the extensive attention of researchers. Lefkowitz *et al.* have used the schlieren imaging and optical emission spectra to reveal the evolution characteristics during and between the discharge pulses for the nanosecond repetitively pulsed discharge in CH_4/air.[14] Levko and Raja have studied the active species production by the CH_4/air streamer discharge and have concluded that steamers initiated by the positive and negative trigger voltage cannot be considered symmetrical.[15] More recently, Qian *et al.* have presented a fluid modeling study of the radical species generation

a)Author to whom correspondence should be addressed: sdnupanjie@163.com

by a positive streamer in the dense CH_4/air DBD.[16] Specific experimental study and numerical simulation that concentrate on the CH_4 conversion in the nanosecond pulsed needle-plane discharge plasma have been less reported so far.

Both spatial-temporal evolution characteristics of particle densities and reaction pathways of producing and losing particles in the non-equilibrium discharge plasma have been long-lasting academic hotspots.[17–23] For the atmospheric pressure methane discharge plasma, the *in-situ* and real-time diagnosis methods for particle densities are still rare, and therefore numerical simulation becomes an alternative way to study the above issues. Using a zero-dimensional (global) model, Wang *et al*. have investigated the effects of changing CH_4/Ar mole ratio, feed flow rate, input voltage, and reactor configuration on the direct conversion of methane into higher hydrocarbons in a DBD microplasma reactor.[24] Kimura and Kasugai have investigated the particle densities of inductively coupled radio frequency CH_4/H_2 plasmas by combining experiments with global model.[25] Recently, Levko and Raja have compared fluid and global models for the simulation of active species produced by atmospheric pressure streamer discharge in CH_4/air and have obtained good agreement between the fluid and global models.[15] In addition, the comprehensive two-dimensional fluid models have been successfully developed to numerically study CH_4 reforming.[26–28] Herrebout *et al*. have compared a one-dimensional and a two-dimensional self-consistent fluid models for the CH_4 radio frequency plasma and have shown that the calculation results obtained with the two models are in relatively good agreement.[26] Babaeva *et al*. have used the two-dimensional simulator to research the interaction between plasma filaments in DBDs and liquid covered wounds.[27] Levko *et al*. have studied non-thermal plasma ethanol reforming in argon bubbles immersed in liquids using a two-dimensional multi-species fluid model and have analyzed the main reactions responsible for the generation of molecular hydrogen and light hydrocarbon species.[28] The self-consistent two-dimensional numerical model on the nanosecond time scale should be developed to further research the reaction pathway contributions and mechanisms of producing and losing particles in the methane nanosecond pulsed needle-plane discharge plasma.

The objective of this work is to illustrate the key reaction pathways of generating and consuming various kinds of particles in the methane discharge plasma excited by the nanosecond pulsed voltage. A two-dimensional fluid model is built up to simulate the atmospheric pressure methane plasma and quantitatively research the yields and contributions of each reaction. The rest of this manuscript is organized as follows: The simulation model is introduced in Sec. II. Based on the systematic calculations and analyses of the generation and loss reaction yields for all kinds of particles considered in the simulation model, the reaction pathway maps of producing and losing particles are presented in Sec. III. Finally, the conclusions are summarized in Sec. IV.

II. SIMULATION MODEL

Figure 1 presents (a) experimental setup and (b) schematic diagram of the modeling geometry of the nanosecond pulsed needle-plane discharge in methane at atmospheric pressure.

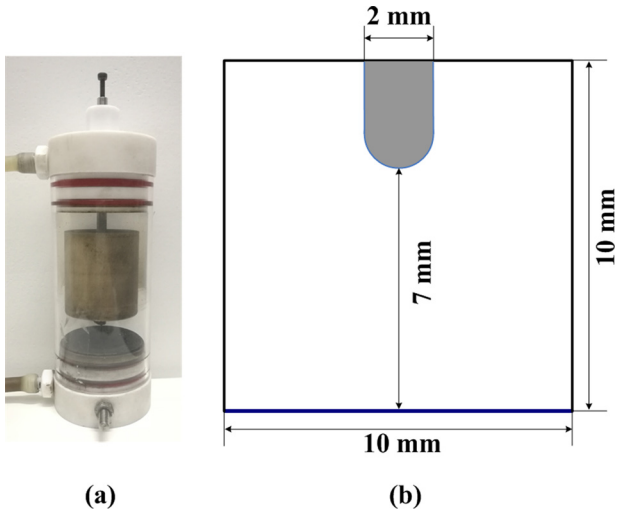

FIG. 1. (a) Experimental setup and (b) schematic diagram of the modeling geometry of the nanosecond pulsed needle-plane discharge in methane at atmospheric pressure.

The geometry of the simulation model is set to be the same as that of the experimental setup of institute of electrical engineering, Chinese academy of sciences. In the present simulation model, the size of the calculation region is 10 mm × 10 mm. Diameter and needle tip curvature radius of the metal (tungsten) needle electrode are 2 mm and 1 mm, respectively. The distance between the head of the needle electrode and the upper surface of the metal (copper) plane electrode is 7 mm. Furthermore, the needle electrode is connected to the positive nanosecond pulsed voltage and the plane electrode is ground electrode. Figure 2 shows the waveforms of supply voltage recorded by the oscilloscope and simulation voltage used in the model.

In order to improve the computational efficiency, only 19 key particles and 80 main reactions are considered in the simulation model. The 19 particles include background molecules CH_4, neutral particles CH_3, CH_2, CH, C, H_2, H, C_2H_2, and C_2H_4, electrons e, and ions CH_4^+, CH_3^+, CH_2^+, CH^+, C^+, H^+, H_2^+, $C_2H_2^+$, and $C_2H_4^+$. The main reactions taken into account in the simulation model and the reaction rate coefficients as well as the corresponding references are listed in Table I. It should be pointed out that the reaction

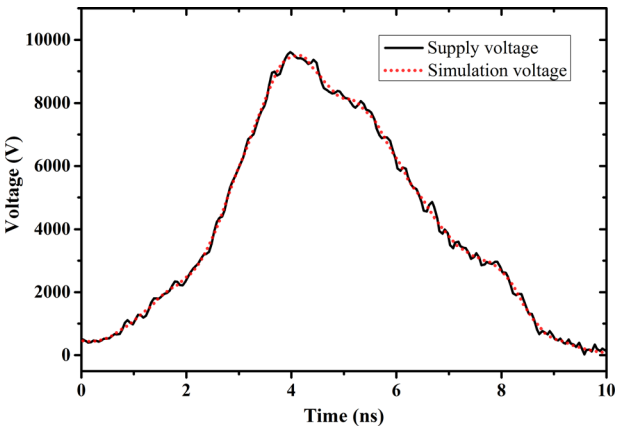

FIG. 2. Waveforms of supply voltage recorded by the oscilloscope and simulation voltage used in the model.

TABLE I. Main reactions used in the simulation model and reaction rate coefficients as well as the corresponding references.

Reaction No.	Reaction equation	Reaction rate coefficient[a, b]	References
R01	$e + CH_4 \rightarrow CH_4 + e$	σ[c]	32
R02	$e + CH_4 \rightarrow CH_4^+ + 2e$	σ[c]	32
R03	$e + CH_4 \rightarrow CH_3^+ + H + 2e$	σ[c]	32
R04	$e + CH_4 \rightarrow CH_2 + H_2 + e$	σ[c]	32
R05	$e + CH_4 \rightarrow CH_3 + H + e$	σ[c]	32
R06	$e + C_2H_4 \rightarrow C_2H_2 + H_2 + e$	σ[c]	32
R07	$e + H_2 \rightarrow H_2^+ + 2e$	σ[c]	32
R08	$e + CH_4 \rightarrow CH + 3H + e$	$2.07 \times 10^{-14}\exp(-11.7/T_e)$	25
R09	$e + CH_4 \rightarrow C + 4H + e$	$2.29 \times 10^{-14}\exp(-12.6/T_e)$	25
R10	$e + CH_3 \rightarrow CH_2 + H + e$	$4.1\times 10^{-14}\exp(-11.3/T_e)$	25
R11	$e + CH_3 \rightarrow CH + 2H + e$	$1.69 \times 10^{-14}\exp(-10.3/T_e)$	25
R12	$e + CH_2 \rightarrow CH + H + e$	$2.37\times 10^{-14}\exp(-11.3/T_e)$	25
R13	$e + CH_2 \rightarrow C + 2H + e$	$9.77 \times 10^{-14}\exp(-10.3/T_e)$	25
R14	$e + CH \rightarrow C + H + e$	$1.94 \times 10^{-14}\exp(-11.3/T_e)$	25
R15	$e + C_2H_4 \rightarrow C_2H_2 + 2H + e$	$4.13 \times 10^{-14}\exp(-10.3/T_e)$	25
R16	$e + CH_3 \rightarrow CH_3^+ + 2e$	$2.35 \times 10^{-14}\exp(-14.7/T_e)$	25
R17	$e + CH_3 \rightarrow CH_2^+ + H + 2e$	$1.62 \times 10^{-14}\exp(-17.0/T_e)$	25
R18	$e + CH_2 \rightarrow CH_2^+ + 2e$	$2.35 \times 10^{-14}\exp(-14.7/T_e)$	25
R19	$e + CH_2 \rightarrow CH^+ + H + 2e$	$1.21 \times 10^{-14}\exp(-20.5/T_e)$	25
R20	$e + CH \rightarrow CH^+ + 2e$	$2.35 \times 10^{-14}\exp(-14.7/T_e)$	25
R21	$e + CH \rightarrow C^+ + H + 2e$	$5.57 \times 10^{-15}\exp(-19.6/T_e)$	25
R22	$e + C \rightarrow C^+ + 2e$	$4 \times 10^{-14}\exp(-12.6/T_e)$	25
R23	$e + C_2H_2 \rightarrow C_2H_2^+ + 2e$	$3.73 \times 10^{-14}\exp(-12.2/T_e)$	25
R24	$e + C_2H_4 \rightarrow C_2H_2^+ + H_2 + 2e$	$5.12 \times 10^{-14}\exp(-14.1/T_e)$	25
R25	$e + CH_2^+ \rightarrow CH + H$	$2.5 \times 10^{-13}(300/T_e)^{0.5}$	33
R26	$e + C_2H_4^+ \rightarrow C_2H_2 + 2H$	2×10^{-33}	25
R27	$C^+ + CH_4 \rightarrow C_2H_2^+ + H_2$	4×10^{-16}	25
R28	$C^+ + CH_3 \rightarrow C_2H_2^+ + H$	1.3×10^{-15}	29
R29	$C^+ + CH_2 \rightarrow CH_2^+ + C$	5.2×10^{-16}	29
R30	$C^+ + CH \rightarrow CH^+ + C$	3.8×10^{-16}	29
R31	$C^+ + C_2H_4 \rightarrow C_2H_4^+ + C$	1.7×10^{-17}	29
R32	$C_2H_2^+ + C_2H_4 \rightarrow C_2H_4^+ + C_2H_2$	4.14×10^{-16}	29
R33	$CH^+ + CH_4 \rightarrow C_2H_4^+ + H$	6.5×10^{-17}	29
R34	$CH^+ + CH_4 \rightarrow C_2H_2^+ + H_2 + H$	1.43×10^{-16}	29
R35	$CH^+ + H_2 \rightarrow CH_2^+ + H$	1.2×10^{-15}	29
R36	$CH^+ + H \rightarrow C^+ + H_2$	7.5×10^{-16}	29
R37	$CH_2^+ + CH_4 \rightarrow C_2H_2^+ + 2H_2$	3.97×10^{-16}	25
R38	$CH_2^+ + CH_4 \rightarrow C_2H_4^+ + H_2$	8.4×10^{-16}	25
R39	$CH_2^+ + H_2 \rightarrow CH_3^+ + H$	1.6×10^{-15}	25
R40	$CH_2^+ + CH_4 \rightarrow CH_3^+ + CH_3$	1.38×10^{-16}	29
R41	$CH_3^+ + CH_4 \rightarrow CH_4^+ + CH_3$	1.36×10^{-16}	25
R42	$CH_3^+ + CH \rightarrow C_2H_2^+ + H_2$	7.1×10^{-16}	29
R43	$CH_4^+ + C_2H_4 \rightarrow C_2H_4^+ + CH_4$	1.38×10^{-15}	29
R44	$CH_4^+ + C_2H_2 \rightarrow C_2H_2^+ + CH_4$	1.13×10^{-15}	29
R45	$CH_4^+ + H \rightarrow CH_3^+ + H_2$	1×10^{-17}	29
R46	$H^+ + CH_4 \rightarrow CH_4^+ + H$	1.5×10^{-15}	29
R47	$H^+ + CH_4 \rightarrow CH_3^+ + H_2$	2.3×10^{-15}	29
R48	$H^+ + CH_3 \rightarrow CH_3^+ + H$	3.4×10^{-15}	29
R49	$H^+ + CH_2 \rightarrow CH_2^+ + H$	1.4×10^{-15}	29
R50	$H^+ + CH_2 \rightarrow CH^+ + H_2$	1.4×10^{-15}	29
R51	$H^+ + CH \rightarrow CH^+ + H$	1.9×10^{-15}	29
R52	$H^+ + C_2H_4 \rightarrow C_2H_4^+ + H$	1×10^{-15}	29
R53	$H^+ + C_2H_4 \rightarrow C_2H_2^+ + H_2 + H$	1×10^{-15}	29
R54	$H^+ + C_2H_2 \rightarrow C_2H_2^+ + H$	5.4×10^{-16}	29
R55	$H_2^+ + CH_4 \rightarrow CH_4^+ + H_2$	1.4×10^{-15}	29
R56	$H_2^+ + CH_4 \rightarrow CH_3^+ + H_2 + H$	2.3×10^{-15}	29
R57	$H_2^+ + CH_2 \rightarrow CH_3^+ + H$	1×10^{-15}	29
R58	$H_2^+ + CH_2 \rightarrow CH_2^+ + H_2$	1×10^{-15}	29
R59	$H_2^+ + CH \rightarrow CH_2^+ + H$	7.1×10^{-16}	29
R60	$H_2^+ + CH \rightarrow CH^+ + H_2$	7.1×10^{-16}	29

TABLE I. (*Continued*.)

Reaction No.	Reaction equation	Reaction rate coefficient[a, b]	References
R61	$H_2^+ + C \rightarrow CH^+ + H$	2.4×10^{-15}	29
R62	$H_2^+ + C_2H_4 \rightarrow C_2H_4^+ + H_2$	2.21×10^{-15}	29
R63	$H_2^+ + C_2H_4 \rightarrow C_2H_2^+ + 2H_2$	8.82×10^{-16}	29
R64	$H_2^+ + C_2H_2 \rightarrow C_2H_2^+ + H_2$	4.82×10^{-15}	29
R65	$H_2^+ + H \rightarrow H^+ + H_2$	6.4×10^{-16}	29
R66	$CH + CH \rightarrow C_2H_2$	2×10^{-16}	25
R67	$CH + CH_2 \rightarrow C_2H_2 + H$	6.6×10^{-17}	25
R68	$CH + CH_4 \rightarrow C_2H_4 + H$	1×10^{-16}	25
R69	$CH + H \rightarrow C + H_2$	4.98×10^{-17}	25
R70	$H_2 + CH \rightarrow CH_2 + H$	3.03×10^{-17}	25
R71	$CH_2 + CH_2 \rightarrow C_2H_2 + H_2$	$2 \times 10^{-16}\exp(-400/T_g)$	25
R72	$CH_2 + CH_2 \rightarrow C_2H_2 + 2H$	5.27×10^{-17}	29
R73	$CH_2 + CH_2 \rightarrow C_2H_4$	1.7×10^{-18}	25
R74	$CH_3 + CH_2 \rightarrow C_2H_4 + H$	7×10^{-17}	25
R75	$CH_3 + CH_3 \rightarrow C_2H_4 + H_2$	$1.7 \times 10^{-14}\exp(-16000/T_g)$	25
R76	$C + CH_4 \rightarrow C_2H_2 + H_2$	1×10^{-17}	25
R77	$H + CH_2 \rightarrow CH + H_2$	$1 \times 10^{-17}\exp(-900/T_g)$	25
R78	$H + CH_3 \rightarrow CH_2 + H_2$	$1 \times 10^{-16}\exp(-7600/T_g)$	25
R79	$CH_3 + H \rightarrow CH_4$	7×10^{-18}	25
R80	$H + CH_4 \rightarrow CH_3 + H_2$	$2.2 \times 10^{-26}T_g^3\exp(-4045/T_g)$	25

[a]The unit of the reaction rate coefficients is $m^3\ s^{-1}$.
[b]T_e is the electron temperature in eV and T_g is the gas temperature in K.
[c]Calculated by Bolsig+ using cross sections from LXcat database.

mechanism in this work is simplified. The higher order neutral molecules and positive ions, such as C_2H_6, C_3H_6, C_3H_8, $C_2H_5^+$, and $C_2H_6^+$, and the more abundant gas phase chemistry reactions in the CH_4 plasma have been considered in the simulation model.[29] In addition, Starik *et al*. have established the complete reaction mechanisms in CH_4/O_2 and CH_4/air.[30,31] Electron densities and electron temperatures calculated by the present model are slightly higher than the simulation results in Ref. 29, which should be attributed to the difference between the needle-plane discharge and the DBD. The rate coefficients of reactions R08–R24 are the expressions taken from Ref. 25. The more accurate rate coefficients of these reactions can be calculated by Bolsig+ in analogy to the rate coefficients of reactions R01–R07. The improved reaction rate coefficients based on cross sections will be taken into account in the future work to optimize the simulation model.

The two-dimensional fluid model is built up to simulate the atmospheric pressure methane needle-plane discharge plasma driven by the nanosecond pulsed voltage. The basic governing equations of the fluid model consist mainly of the continuity equation, the Poisson's equation, and the electron energy conservation equation.

The continuity equation is expressed as

$$\frac{\partial n_{e,i,np}}{\partial t} + \nabla \cdot \boldsymbol{\Gamma}_{e,i,np} = \boldsymbol{S}_{e,i,np}, \tag{1}$$

where n is the particle number density, $\boldsymbol{\Gamma}$ is the particle flux density, $\boldsymbol{S}$ represents the sources and losses of the particles, and subscripts e, i, and np denote electron, ion, and neutral particles, respectively.

The electric field intensity $\boldsymbol{E}$ is determined by the Poisson's equation, taking the form of

$$\boldsymbol{E} = -\nabla\varphi, \tag{2}$$

$$\nabla \cdot (\varepsilon_0\varepsilon_r\nabla\varphi) = -e\sum q_{e,i}n_{e,i}, \tag{3}$$

where φ is the scalar electric potential, ε_0 is the vacuum permittivity, ε_r is the relative permittivity, e is the electron charge, and q stands for electric quantity of the charged particle.

The background gas temperature T_g is set to 350 K and the electron temperature T_e is calculated by the following electron energy conservation equation:

$$\frac{\partial}{\partial t}\left(\frac{3}{2}K_B T_e n_e\right) + \nabla \cdot \boldsymbol{\Psi}_e = -\left(\frac{3K_B m_e}{eM_k}\right)n_e\nu_{el}(T_e - T_g) - \sum \Delta\varepsilon_i r_i - \sum \boldsymbol{\Gamma}_e \cdot \boldsymbol{E}, \tag{4}$$

where K_B is the Boltzmann constant, $\boldsymbol{\psi}_e$ is the electron energy flux, m_e is the electron mass, M_k is the molecule mass of the kth species, ν_{el} is the relative speed of the elastic collision, $\Delta\varepsilon_i$ is the energy loss per electron in an inelastic collision event caused by the ith reaction, and r_i is the reaction rate of the ith reaction.

$\boldsymbol{\psi}_e$ is obtained from

$$\boldsymbol{\Psi}_e = -\lambda_e\nabla T_e + \frac{5}{2}K_B T_e \boldsymbol{\Gamma}_e. \tag{5}$$

λ_e is further given by

$$\lambda_e = \frac{5}{2}K_B D_e n_e, \tag{6}$$

where D_e is the diffusion coefficient of the electron. In this simulation model, D_e is calculated by the Boltzmann equation solver Bolsig+.[32]

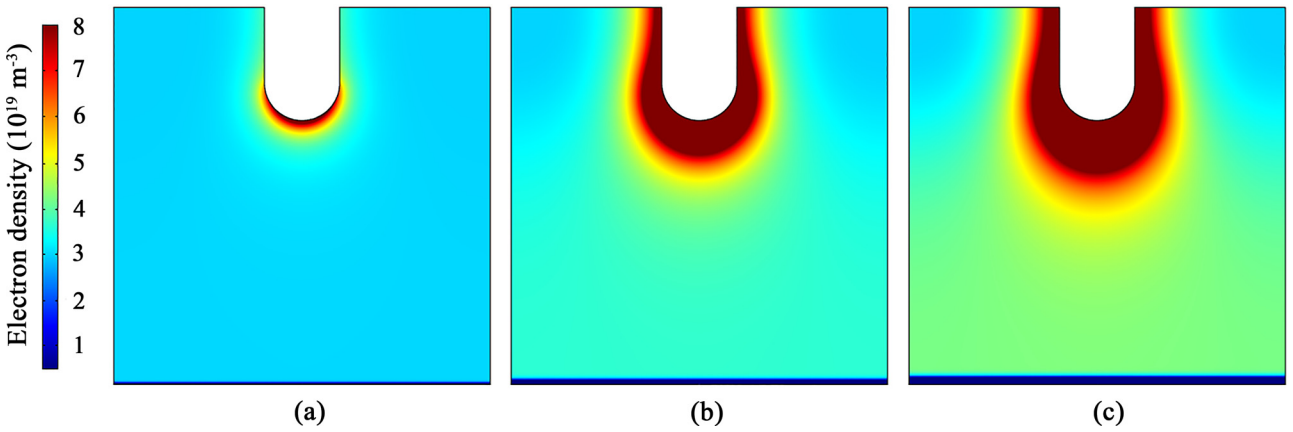

FIG. 3. Spatial distributions of electron densities at (a) 3 ns, (b) 5 ns, and (c) 7 ns of the applied voltage.

The complete absorption at the surface of the wall is used as the boundary conditions for ions and neutral particles. Electrons at the surface are gained due to the secondary electron emissions caused by the ion impinging, and the secondary electron emission coefficient is set as 0.01.

Comsol 5.1 is carried out to generate mesh and accomplish numerical calculation. In the calculation region, the axial symmetric structure and the non-uniform triangular meshes are utilized. The mesh number is 19 894 and the degree of freedom is 296 600. The degree of freedom is approximately equal to the product of the number of nodes and the number of dependent variables per node. The uniform distributions of the modeled particles are used as initial conditions, and the initial densities of all types of neutral particles, positive ions, and electrons are set as $1 \times 10^{8}\,\mathrm{m}^{-3}$, $1 \times 10^{13}\,\mathrm{m}^{-3}$, and $9 \times 10^{13}\,\mathrm{m}^{-3}$. The initial electron temperature of is set as 3 eV.

III. RESULTS AND DISCUSSION

Figure 3 gives the spatial distributions of electron densities at (a) 3 ns, (b) 5 ns, and (c) 7 ns of the applied nanosecond pulsed voltage. This figure shows that the electron densities around the needle electrode are obviously higher than the electron densities in other areas of the plasma reactor. It also can be seen that the electron densities near the needle electrode continuously increase in the duration of the positive nanosecond pulsed voltage.

The spatial distributions of electron temperatures at (a) 3 ns, (b) 5 ns, and (c) 7 ns are shown in Fig. 4. This figure denotes that the electron temperatures near the needle electrode are higher than the electron temperatures in elsewhere of the plasma reactor, which are similar to the spatial distribution characteristics of the electron densities in Fig. 3. On the other side, the temporal evolutions of the electron temperatures in the pulse duration are obviously different with those of the electron densities, that is, the electron temperatures increase during the rising time of the positive pulsed voltage but decrease with the decrease of the applied voltage. Figure 5 shows the time evolutions of the spatial distributions of electric potentials. The increase of the electric field energy causes the increase of the electron temperature at the rising stage of the pulsed voltage and subsequently leads to the continuously electron impact ionizations and the rise of the electron density during the whole voltage pulse.

It has been found that for all investigated CH_4/N_2 ratios in the cylindrical DBD plasma, the maximums of the electron densities are in the order of 10^{18}–$10^{19}\,\mathrm{m}^{-3}$, and the maximums of the electron temperatures are around 3 eV during the pulse,[8] which are typical conditions for the DBD at atmospheric pressure and obviously lower than the simulation results of the nanosecond pulsed needle-plane discharge calculated by the present model.

Figure 3(c) illustrates that the electron densities in the area between the metal needle electrode and the plane electrode at

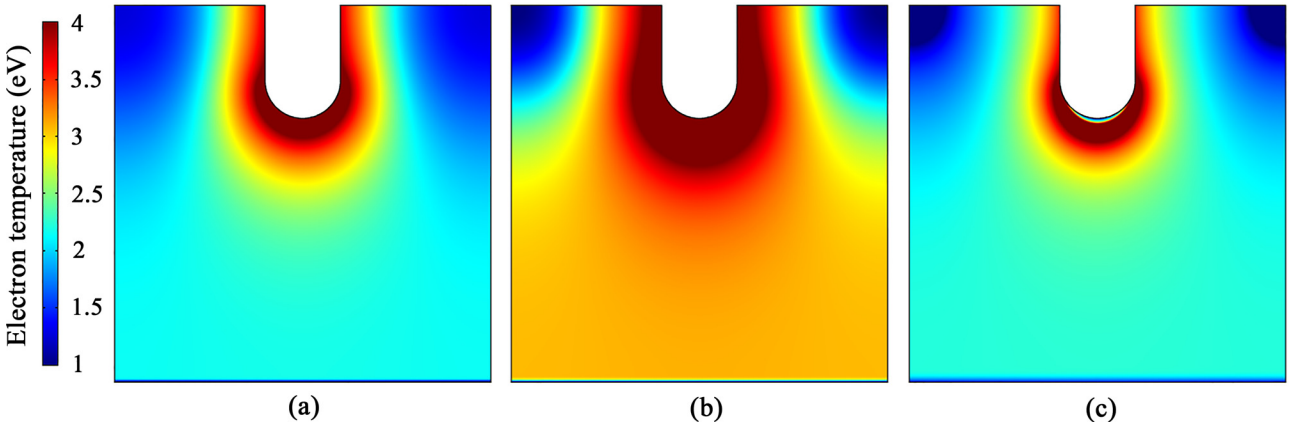

FIG. 4. Spatial distributions of electron temperatures at (a) 3 ns, (b) 5 ns, and (c) 7 ns of the applied voltage.

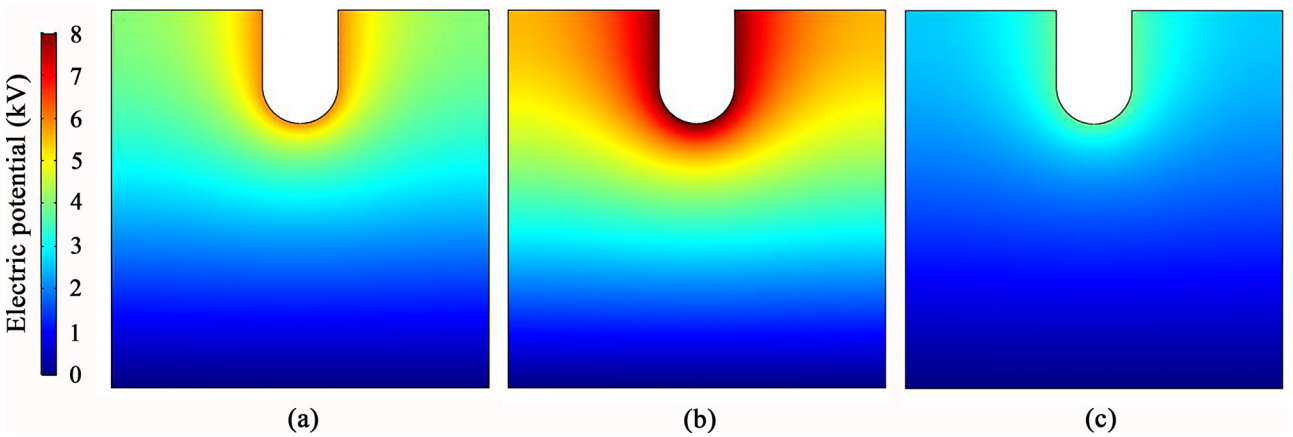

FIG. 5. Spatial distributions of electric potentials at (a) 3 ns, (b) 5 ns, and (c) 7 ns of the applied voltage.

7 ns of the applied voltage are higher than $3 \times 10^{19}\,m^{-3}$, which means that the streamer has bridged the cathode-anode gap. The streamer head, body, and tail cannot be distinguished in the present simulation results. The mechanisms of the initiation and propagation for the streamer can be described as follows.[34] Since the dense quasi-neutral plasma of the streamer body screens the applied voltage, the largest voltage drop and the local enhancement of the electric field occur between the streamer head and the cathode.[15] The enhanced electric field accelerates the electrons to move toward the streamer head and causes electron/ion multiplication.[35] Subsequently, the energetic electrons compensate the positive space charge of the streamer head and leave the uncompensated ion charges, which promotes the fast streamer propagation to the cathode.

On the basis of the aforementioned two-dimensional fluid model, the yields of 80 reactions listed in Table I are calculated, and the quantitative contributions of these reactions to generate and consume all kinds of particles are systematically researched. Figure 6 shows reaction yields of $e + CH_4 \rightarrow CH_4^+ + 2e$ (R02 in Table I) at (a) 3 ns, (b) 5 ns, and (c) 7 ns of the applied voltage. The reaction yield is the product of the particle densities and the corresponding reaction rate coefficient. The total reaction yield is the time and space accumulative result of the reaction fields for each space grid and time step. The contribution of the reaction is the percentage ratio of the yield for one kind of particle resulted from one reaction to the total yield for this particle produced by all the relevant reaction pathways.

The reaction pathway maps or the key reactions of generating and losing dominant neutral particles are shown in Table II. The reactions exist in the table means that the yield of the reaction is more than 99.99% of the total yield for the corresponding particle. In Figs. 7–12, the solid lines and the dotted lines stand for the major reactions (reaction contribution is more than 10%) and the minor reactions, respectively. Another kind of particle participated in the reaction, the reaction no. in Table I, and the proportion of the reaction yield are displayed in the middle of the lines.

It can be seen from Table II and Figs. 7–12 that CH_2 and CH mainly come from the electron collisions with CH_4. The reactions between the neutral particles and CH_4 are the essential pathways to produce other neutral particles. 99.89% of CH_3 and 98.18% of H_2 derive from the reaction between H and CH_4, that is, $H + CH_4 \rightarrow CH_3 + H_2$. The reaction between CH and CH_4, namely, $CH + CH_4 \rightarrow C_2H_4 + H$, produces 93.63% of H and the majority of C_2H_4. The reaction $C + CH_4 \rightarrow C_2H_2 + H_2$ is the dominated reaction pathway to produce C_2H_2. In addition, the electron collisions with CH_4 also generate a small amount of the neutral particles CH_3, CH_2, and H.

It has been illustrated that in the streamer head of the CH_4/air plasma, the dominant reaction of H generation is the

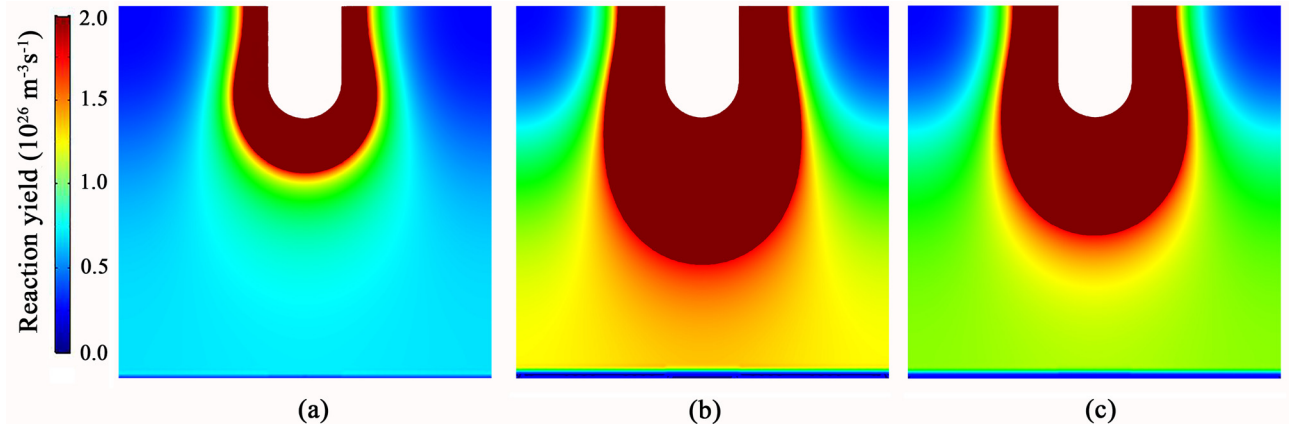

FIG. 6. Spatial distributions of reactions yields of the reaction $e + CH_4 \rightarrow CH_4^+ + 2e$ (R02 in Table I) at (a) 3 ns, (b) 5 ns, and (c) 7 ns of the applied voltage.

TABLE II. Reaction pathway maps or the key reactions of generating and losing dominant neutral particles.

Particle	CH_3	CH_2[a]	CH[a, b]	H_2	H[b]	C_2H_2	C_2H_4
Produce	Figure 7	Figure 8	Figure 9	Figure 10	Figure 11	R76	R68
Loss	R79	Figure 12	R68	R70	R80	R44	R43

[a]The particle is primarily generated by the electron collision with CH_4.
[b]The particle is primarily consumed by the reaction between itself and CH_4.

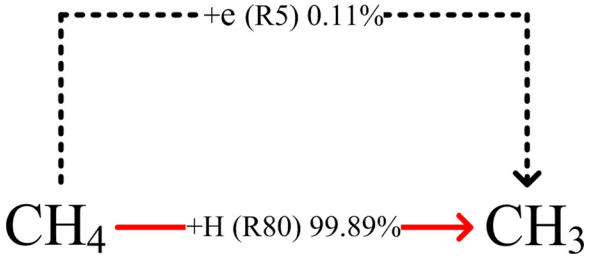

FIG. 7. Pathway map of producing CH_3.

FIG. 8. Pathway map of producing CH_2.

FIG. 9. Pathway map of producing CH.

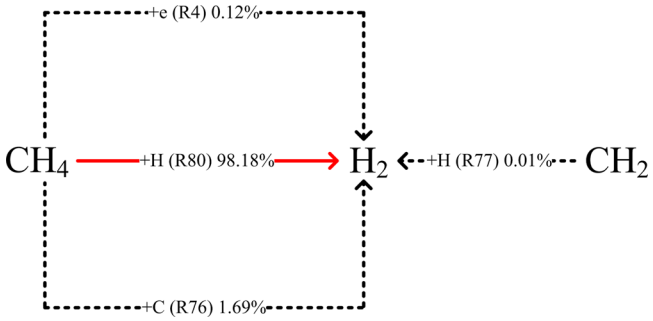

FIG. 10. Pathway map of producing H_2.

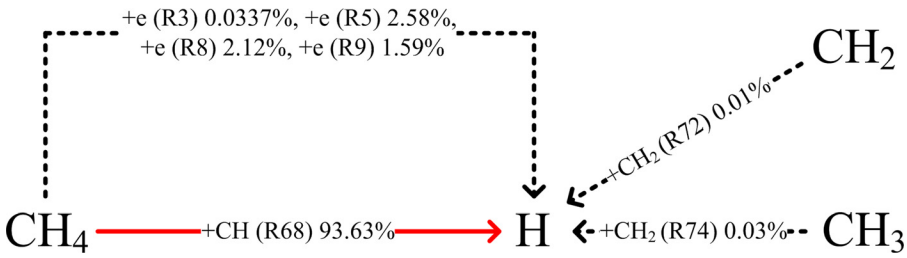

FIG. 11. Pathway map of producing H.

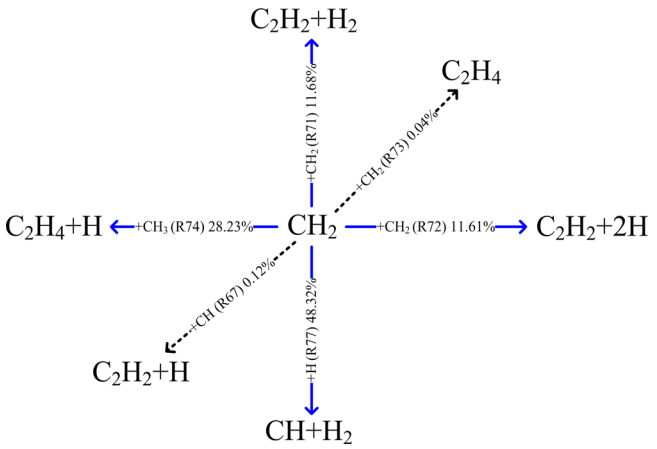

FIG. 12. Pathway map of losing CH_2.

electron impact dissociation of CH_4, due to the high electron temperature at the streamer head.[15] And therefore, $CH + CH_4 \rightarrow C_2H_4 + H$ (R68 in Table I) is only the dominated mechanism of producing H atoms in the streamer body and tail. In the present work, the total reaction yields are the accumulative results of the reaction fields for each space grid and time step, so that the reaction R68 produces the majority of H for the whole calculation region and applied voltage period. It is noted that the accurate H generation mechanism should be modified based on the correct cross section, but the electron impact dissociation cross sections of R08 and R09 are absent in Bolsig+ and have been less reported in the literature.

For the CH and H, the reactions between them and background gas molecules CH_4 contribute to the substantial losses of these particles, and the corresponding reactions are $CH + CH_4 \rightarrow C_2H_4 + H$ and $H + CH_4 \rightarrow CH_3 + H_2$. The key reaction pathways responsible for the losses of the particles CH_3 and H_2 are $CH_3 + H \rightarrow CH_4$ and $H_2 + CH \rightarrow CH_2 + H$, respectively. For the losses of CH_2, the relevant reaction pathways are complicated, as shown in Fig. 12. The reactions between CH_2 and themselves, H, and CH_3 are all the important pathways for the losses of CH_2. As to the hydrocarbons C_2H_2 and C_2H_4, the charge transfer reactions, including $CH_4^+ + C_2H_2 \rightarrow C_2H_2^+ + CH_4$ and $CH_4^+ + C_2H_4 \rightarrow C_2H_4^+ + CH_4$, are the major reactions responsible for their losses.

It should be noted that H_2 converted from CH_4 can be used for the processing of fossil fuels and the productions of ammonia and methanol. It has been found that H_2 is primarily generated by the electron impact dissociations of the hydrocarbon molecules, such as C_2H_6 and C_3H_8, and is mainly lost by the electron impact dissociation reaction $e + H_2 \rightarrow 2H + e$.[29] The higher hydrocarbon molecules C_xH_y ($y \geq 5$) and more completed electron impact dissociation

reactions will be taken into account in the future work to further optimize the simulation model.

Following the same rules with Table II, Table III shows the reaction pathway maps or the key reactions of generating and losing dominant charged particles. From Table III and Figs. 13–18, it can be sum up that:

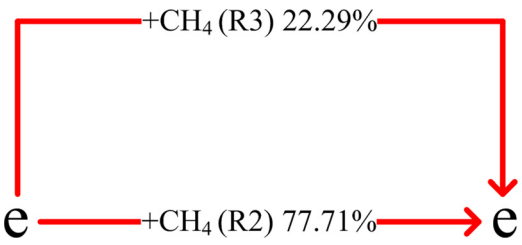

FIG. 13. Pathway map of producing e.

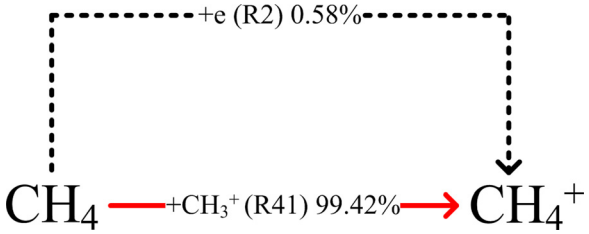

FIG. 14. Pathway map of producing CH_4^+.

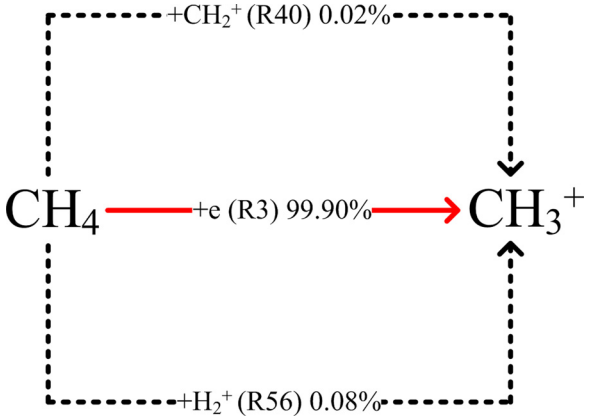

FIG. 15. Pathway map of producing CH_3^+.

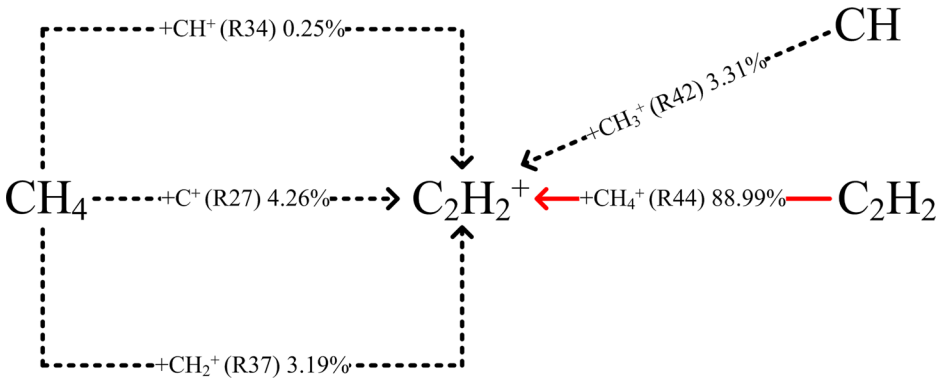

FIG. 16. Pathway map of producing $C_2H_2^+$.

TABLE III. Reaction pathway maps or the key reactions of generating and losing dominant charged particles.

Particle	e[a]	CH_4^+	$CH_3^{+a,b}$	$C_2H_2^+$	$C_2H_4^+$
Produce	Figure 13	Figure 14	Figure 15	Figure 16	Figure 17
Loss	R25	Figure 18	R41	R32	R26

[a]The particle is primarily generated by the electron collision with CH_4.
[b]The particle is primarily consumed by the reaction between itself and CH_4.

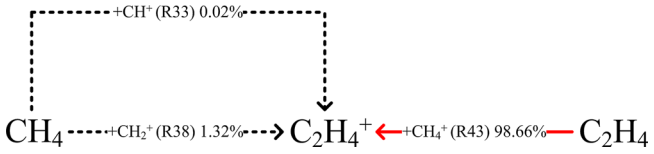

FIG. 17. Pathway map of producing $C_2H_4^+$.

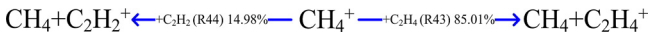

FIG. 18. Pathway map of losing CH_4^+.

The electron impact ionization reactions, including $e + CH_4 \rightarrow CH_4^+ + 2e$ (77.71% for e) and $e + CH_4 \rightarrow CH_3^+ + H + 2e$ (22.29% for e), produce the majority of the electrons and CH_3^+. The ions CH_4^+ are primarily generated by the charge transfer reactions $CH_3^+ + CH_4 \rightarrow CH_4^+ + CH_3$. The charge transfer reactions $CH_4^+ + C_2H_2 \rightarrow C_2H_2^+ + CH_4$ and $CH_4^+ + C_2H_4 \rightarrow C_2H_4^+ + CH_4$ are the key pathways to produce $C_2H_2^+$ and $C_2H_4^+$.

The electrons are mainly lost by the reaction $e + CH_2^+ \rightarrow CH + H$. The positive ions CH_4^+ are lost through two pathways $CH_4^+ + C_2H_4 \rightarrow C_2H_4^+ + CH_4$ (85.01% for CH_4^+) and $CH_4^+ + C_2H_2 \rightarrow C_2H_2^+ + CH_4$ (14.98% for CH_4^+). The reactions between the background gas molecules CH_4 and the ions CH_3^+ are the dominated losing pathways of the ions. The charge transfer reaction $C_2H_2^+ + C_2H_4 \rightarrow C_2H_4^+ + C_2H_2$ and the dissociative electron-ion recombination reaction $e + C_2H_4^+ \rightarrow C_2H_2 + 2H$ are the significant pathways of losing $C_2H_2^+$ and $C_2H_4^+$.

IV. CONCLUSION

In this work, a two-dimensional fluid model is built up to numerically investigate the atmospheric pressure methane nanosecond pulsed needle-plane discharge plasma. The

yields of the 80 reactions and the contributions of these reactions to the densities of the 18 particles in the methane discharge plasma are systematically calculated and studied. The simulation results show that the electron collisions with the background gas molecules CH_4 are the dominated pathways to generate the neutral particles CH_2 and CH and the charged particles e and CH_3^+. The other neutral particles, including CH_3, H_2, H, C_2H_2, and C_2H_4, primarily result from the reactions between these neutral particles and CH_4. The charge transfer reactions are the main pathways to generate the ions CH_4^+, $C_2H_2^+$, and $C_2H_4^+$. As to the neutral particles CH and H as well as the positive ions CH_3^+, the reactions between them and CH_4 contribute to substantial losses of these particles. The important pathways for the losses of CH_3, H_2, C_2H_2, and C_2H_4 are $CH_3 + H \rightarrow CH_4$, $H_2 + CH \rightarrow CH_2 + H$, $CH_4^+ + C_2H_2 \rightarrow C_2H_2^+ + CH_4$, and $CH_4^+ + C_2H_4 \rightarrow C_2H_4^+ + CH_4$. CH_4^+ are mainly consumed by $CH_4^+ + C_2H_4 \rightarrow C_2H_4^+ + CH_4$ and $CH_4^+ + C_2H_2 \rightarrow C_2H_2^+ + CH_4$. Electrons and $C_2H_4^+$ are lost by the dissociative electron-ion recombination reactions. The essential consumption reaction of $C_2H_2^+$ is the charge transfer reaction.

ACKNOWLEDGMENTS

This work was supported by the National Natural Science Foundation of China (Grant No. 51707111) and the Key Research and Development Plan of Shandong Province (Grant No. 2016GGX101016).

[1]A. Mohanta, B. Lanfant, M. Asfaha, and M. Leparoux, Appl. Phys. Lett. **110**, 093109 (2017).
[2]W. Wang, D. Mei, X. Tu, and A. Bogaerts, Chem. Eng. J. **330**, 11 (2017).
[3]M. Laroussi, X. Lu, and M. Keidar, J. Appl. Phys. **122**, 020901 (2017).
[4]A. M. Lietz, E. Johnsen, and M. J. Kushner, Appl. Phys. Lett. **111**, 114101 (2017).
[5]T. Shao, W. Yang, C. Zhang, Z. Niu, P. Yan, and E. Schamiloglu, Appl. Phys. Lett. **105**, 071607 (2014).
[6]R. Wang, H. Sun, W. Zhu, C. Zhang, S. Zhang, and T. Shao, Phys. Plasmas **24**, 093507 (2017).
[7]J. Pan, Z. Tan, Y. Liu, G. Pan, and X. Wang, Phys. Plasmas **22**, 093515 (2015).
[8]R. Snoeckx, M. Setareh, R. Aerts, P. Simon, A. Maghari, and A. Bogaerts, Int. J. Hydrogen Energy **38**, 16098 (2013).
[9]X. Tu and J. C. Whitehead, Int. J. Hydrogen Energy **39**, 9658 (2014).
[10]C. D. Bie, J. van Dijk, and A. Bogaerts, J. Phys. Chem. C **119**, 22331 (2015).
[11]J.-L. Liu, H.-W. Park, W.-J. Chung, and D.-W. Park, Plasma Chem. Plasma Process. **36**, 437 (2016).
[12]A. Indarto, Plasma Sources Sci. Technol. **25**, 025002 (2016).
[13]C. Liu, I. Chernets, H. Ji, J. Smith, A. Rabinovich, D. Dobrynin, and A. Fridman, IEEE Trans. Plasma Sci. **45**, 683 (2017).
[14]J. K. Lefkowitz, P. Guo, T. Ombrello, S. H. Won, C. A. Stevens, J. L. Hoke, F. Schauer, and Y. Ju, Combust. Flame **162**, 2496 (2015).
[15]D. Levko and L. L. Raja, Plasma Sources Sci. Technol. **26**, 035003 (2017).
[16]M. Qian, G. Li, J. Knag, S. Liu, C. Ren, J. Zhang, and D. Wang, Phys. Plasmas **25**, 013519 (2018).
[17]J. Pan and L. Li, J. Phys. D: Appl. Phys. **48**, 055204 (2015).
[18]J. Pan, Z. Tan, G. Pan, C. Shan, X. Wang, Y. Liu, and J. Jiang, Phys. Plasmas **23**, 073520 (2016).
[19]A. Barjasteh and E. Eslami, Phys. Plasmas **23**, 033506 (2016).
[20]M. Maulois, M. Ribière, O. Eichwald, M. Yousfi, and B. Azaïs, Phys. Plasmas **23**, 043501 (2016).
[21]B. Ghimire, J. Sornsakdanuphap, Y. J. Hong, H. S. Uhm, K.-D. Weltmann, and E. H. Choi, Phys. Plasmas **24**, 073502 (2017).
[22]R. Wang, K. Zhang, Y. Shen, C. Zhang, W. Zhu, and T. Shao, Plasma Sources Sci. Technol. **25**, 015020 (2016).
[23]J. Duan, X. Lu, and G. He, Phys. Plasmas **24**, 073506 (2017).
[24]B. Wang, W. Yan, W. Ge, and X. Duan, Chem. Eng. J. **234**, 354 (2013).
[25]T. Kimura and H. Kasugai, Jpn. J. Appl. Phys. **51**, 046202 (2012).
[26]D. Herrebout, A. Bogaerts, M. Yan, R. Gijbels, W. Goedheer, and A. Vanhulsel, J. Appl. Phys. **92**, 2290 (2002).
[27]N. Y. Babaeva, W. Tian, and M. J. Kushner, J. Phys. D: Appl. Phys. **47**, 235201 (2014).
[28]D. Levko, A. Sharma, and L. L. Raja, J. Phys. D: Appl. Phys. **50**, 085202 (2017).
[29]C. D. Bie, B. Verheyde, T. Martens, J. van Dijk, S. Paulussen, and A. Bogaerts, Plasma Processes Polym. **8**, 1033 (2011).
[30]A. M. Starik, P. S. Kuleshov, B. I. Loukhovitski, and N. S. Titova, Int. J. Hydrogen Energy **40**, 9872 (2015).
[31]A. M. Starik, P. S. Kuleshov, and N. S. Titova, J. Phys. D: Appl. Phys. **42**, 175503 (2009).
[32]G. J. M. Hagelaar and L. C. Pitchford, Plasma Sources Sci. Technol. **14**, 722 (2005).
[33]J. K. Lefkowitz, P. Guo, A. Rousso, and Y. Ju, Philos. Trans. R. Soc., A **373**, 20140333 (2015).
[34]Y. P. Raizer, *Gas Discharge Physics* (Springer-Verlag, Berlin, 1991).
[35]D. Levko and L. L. Raja, Phys. Plasmas **24**, 124503 (2017).